Geophysical Constraints on the Antarctic Sea Ice Cover

S. V. Nghiem[a, b*], I. G. Rigor[c], P. Clemente-Colón[d], G. Neumann[a], and P. P. Li[a]

[a]Jet Propulsion Laboratory, California Institute of Technology, 4500 Oak Grove Drive, MS 300-235, Pasadena, California 91109, USA. E-mail Son.V.Nghiem@jpl.nasa.gov

[b]Joint Institute for Regional Earth System Science and Engineering, University of California, Los Angeles, California 90095, USA

[c]Applied Physics Laboratory, University of Washington, 1013 NE 40th Street, Box 355640, Seattle, Washington 98105, USA

[d]U.S. National/Naval Ice Center, NOAA Satellite Operations Facility, 4251 Suitland Road, Washington District of Columbia 20395, USA

Key words: Antarctic sea ice, passive and active microwave remote sensing, frontal ice zone, wind patterns, Antarctic Circumpolar Current front, GEBCO bathymetry.

Abstract

The contrast between the slight increase of Antarctic sea ice and the drastic reduction of Arctic sea ice since the 1970s has been a conundrum to be resolved. Sea ice trajectory tracking with satellite scatterometer data in 2008 shows that ice that forms around Antarctica is pushed offshore by katabatic winds influenced by the continental topography. The ice trajectories reveal that sea ice, formed earlier in the ice growth season, drifts northward away from the Antarctic continent forming a circumpolar frontal ice zone (FIZ) behind the ice edge. The FIZ thereby consists of sea ice that becomes rougher due to a longer exposure to wind and wave actions, and thicker over time by more ice growth and greater snow accumulation.

* Corresponding author

In the Antarctic circumpolar sea ice zone adjacent to the sea ice edge, satellite data in 1999-2009 exhibit a band of strong radar backscatter, which is consistent with the signature of older, thicker, and rougher sea ice with more snow in the FIZ. This sea ice band, as wide as 1000 km, serves as a 'Great Shield,' encapsulating and protecting younger and thinner ice in the internal ice pack. In the young and thin ice region behind the FIZ, ice can grow rapidly as winds continue opening interior areas thereby creating effective "ice factories." In addition, ridging can enhance ice thickness by convergence toward the circumpolar FIZ that is recirculated by westerly winds and currents. During the growth season, the FIZ advances until reaching lower-latitude warm waters at a boundary determined by the southern Antarctic Circumpolar Current front that is constrained by seafloor features. These persistent topographical and bathymetric geological factors help sustain the Antarctic sea ice cover. As such, the behavior of Antarctic sea ice is not a paradox as some have suggested, but instead is consistent with the geophysical characteristics in the southern polar region that starkly contrast to those in the Arctic.

1. Introduction

The extent of Antarctic sea ice has increased slightly while Arctic sea ice has diminished drastically in recent decades (IPCC, 2013). This has been cited as a challenging paradox (Walsh, 2009) for which a number of explanations have been suggested, and the inconsistency between simulated and observed changes in Antarctic sea ice remains to be explained (Gagné et al., 2015). Stratospheric ozone depletion may affect atmospheric circulation patterns such as the Southern Annular Mode (SAM), limiting sea surface temperature (SST) change and sustaining the Antarctic sea ice cover (Marshall, 2003; Gillett & Thompson, 2003; Son et al., 2010). However, Sigmond and Fyfe (2010) question the efficacy of ozone depletion on sea ice change

and strongly suggest that processes not linked to stratospheric ozone depletion must be invoked to explain the observation of the small increase in the Antarctic sea ice extent.

Meltwater from Antarctic ice shelves (Rignot et al., 2013) accumulates in a cool and fresh surface layer that cushions the surface ocean from warmer deeper waters leading to an expansion of Antarctic sea ice (Bintanja et al., 2013). The reduction of salinity and density in this near-surface layer may weaken the convective mixing of cold surface water with the underlying warmer water, and thus sustain Antarctic sea ice (Manabe et al., 1991). Moreover, a decrease in sea ice growth may reduce salt rejection and upper-ocean density to enhance thermohaline stratification which suppresses convective overturning, decreases upward heat transport, and thus maintains Antarctic sea ice production (Zhang, 2007). Winds also affect Antarctic sea ice trends (Holland, 2014), and model simulations indicate wind intensification may increase ice production by ridging (Zhang, 2013). As a frozen continent, Antarctica lacks heat sources such as warm river waters, breaking through landfast sea ice held by the regional bathymetry, can effectively melt sea ice as occurs in the Arctic (Nghiem et al., 2014).

In contrast to past studies, this paper presents satellite observations that reveal the formation of a circumpolar frontal ice zone of older, rougher, and thicker sea ice, referred here as a 'Great Shield' zone (GSZ) that in turn protects the Antarctic interior sea ice pack from melting. Also examined are persistent factors that sustain an effective ice growth while maintaining the Antarctic sea ice cover (i.e., decadal trend with a low rate of change of the seasonal maximum extent of the overall Antarctic sea ice cover, typically in late September). The focus here is on the growth season of Antarctic sea ice until its extent reaches the seasonal maximum in September, when the sea ice surface is under freezing conditions without significant melt to obscure satellite signatures of sea ice.

2. Antarctic Sea Ice Change

Antarctic sea ice extent (SIE) retreats to a minimum of 3.1×10^6 km^2 in February, which is just 16.8% of the maximum extent of 18.5×10^6 km^2 in September as observed from multi-decadal satellite data (1979-2013) (Parkinson, 2014). Overall, the Antarctic SIE has a relatively low rate of change since the late 1970s with a slight increase that has not been nearly as large as the decreasing trend of the SIE in the Arctic and not as widespread geographically (Parkinson, 2014). There are also regional differences such as the decrease of sea ice with a shortened ice season in the Bellingshausen Sea region (see Fig.1 for geographical names of seas and locations around Antarctica) in contrast to the late retreat and early advance in the western Ross Sea region (Stammerjohn et al., 2012). Successive Antarctic SIE maximum records in 2012, 2013, and 2014 from satellite observations (Parkinson, 2014; Reid and Massom, 2015), in contrast to record low values of Arctic SIE in March to early June 2015 (*SPIN*, 2015), have further accentuated the polar sea ice differences.

A reliable estimate of the Antarctic snow and sea ice thickness is still elusive (Giles et al., 2008), while there have been some seasonal estimates from Ice, Cloud, and land Elevation Satellite (ICESat) data collected along lines on sea ice surface in different regions at different times in different years (Kurtz & Markus, 2012) with a large range of uncertainty between 20%-80% (Kern & Spreen, 2015). Such fundamental information is crucial for predictive models to attribute observed changes and to assess various impacts (Maksym et al., 2012). Antarctic sea ice properties and growth processes can be quite different from those in the Arctic. With strong wind and wave interactions, Antarctic sea ice is not necessarily limited to thermodynamic growth under quiescent conditions as its thickness can be significantly increased from rafting and ridging (Lewis et al., 2011; Massom et al., 2008) and from heavy snow loading, flooding, and

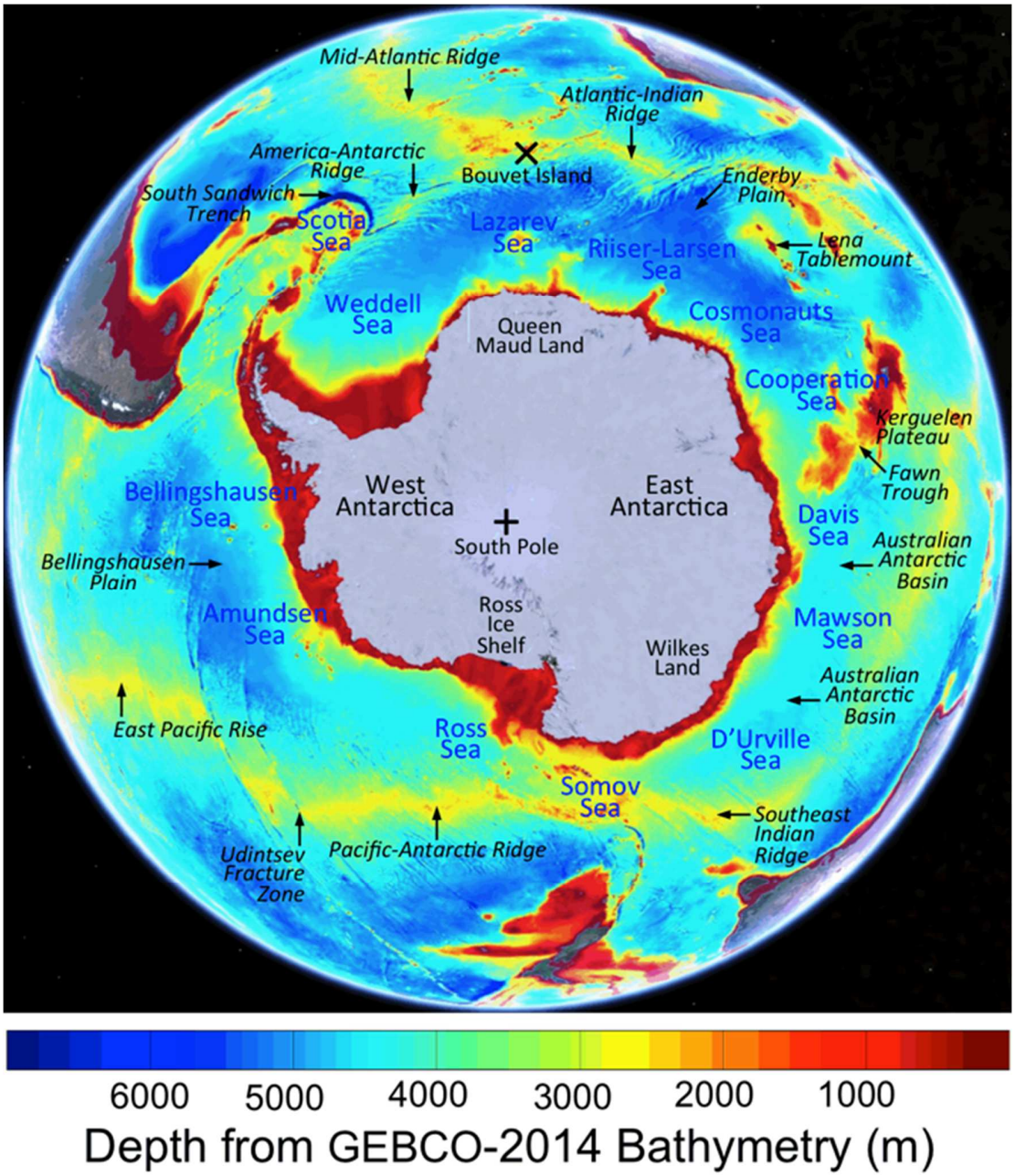

Fig. 1. Names of places on a map of Antarctic land and ocean together with the GEBCO-2014 bathymetry (http://www.gebco.net/data_and_products/gridded_bathymetry_data/).

freezing at the top (Ackley & Sullivan, 1994; Jeffries et al., 1997; Massom et al., 2001). During the ice-growing season, besides the thermodynamic growth, the older sea ice becomes thicker having more time for snow loading through aggregate accumulation and for greater roughness due to a prolonged exposure to high winds and large waves. Therefore, detailed measurements

of snow and ice thickness and other physical properties in various regions of Antarctic sea ice are necessary to identify key dynamic and thermodynamic processes to explain Antarctic sea ice change.

As the thickness information lacks in spatial coverage, revisit frequency, and long-term record, our approach is to utilize observations of the dynamics from sea ice trajectory tracking and from distribution patterns of synoptic sea ice classes from a decade of Ku-band radar data, acquired in 1999-2009 by the SeaWinds scatterometer (a stable and accurate radar) aboard the QuikSCAT satellite. This approach allows an immediate examination of sea ice processes within the SIE from currently available data as a surrogate to the deficient information of Antarctic sea ice thickness distribution.

3. Tracking Sea Ice Trajectories

To examine the evolution of Antarctic sea ice over the growth season (June-September), we implement an algorithm using daily QuikSCAT science data at Level 1B (L1B), accurate to 0.2 dB or 4.7% for 3σ at ~99.7% confidence level (*Tsai et al.*, 2000), to track the dynamics and formation of the different sea ice classes. The active microwave L1B scatterometer data in a posting of 0.25° in latitude and in longitude are provided as input to the tracking algorithm developed specifically for use with the satellite scatterometer observations. These are re-projected into polar coordinates and then interpolated to a rectangular grid with 0.1° spacing using a nearest neighbor scheme. An initial set of points in a 2° grid on sea ice for 1 June 2008 is chosen (Fig. 2a), with associated ice parcels tracked from the sequential rectangular-grid daily L1B data. Year 2008 is selected for this dynamic process study as it was one of the years of exceptional seasonal variability in Antarctic sea ice coverage, which was characterized by three distinctive phases of SIE anomalies and substantial regional variations (Massom et al., 2009), so

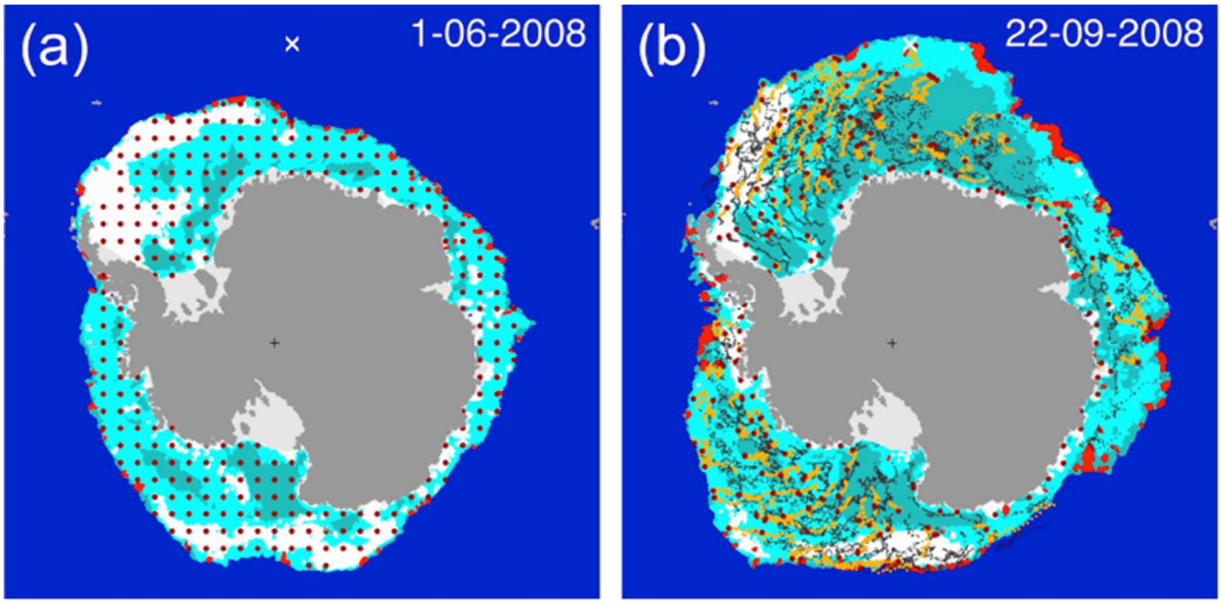

Fig. 2. Tracking of trajectories of sea ice parcels over different synoptic sea ice classes (see definitions in Section 4 and color code in Fig. 4). The left panel (a) represents the initial set of points in a 2° grid on sea ice for 1 June 2008 to track the sea ice parcels associated with this set of points to track their trajectories while no new points are introduced or inserted throughout the tracking process. The right panel (b) shows the trajectories of the sea ice parcels at the end of the tracking on the equinox of 22 September 2008, tracing the entire history of the trajectory of each sea ice parcel from where it started, moved around, reached its final position. Red dots are the current positions of the trajectories on the given date with the orange trails indicating the drift of the tracks during the past 30 days and the trails consisting of small black dots completing all tracking points along the sea ice tracks since 1 June 2008. An animation of the daily sea ice trajectories is presented in Movie 1 at http://urban.jpl.nasa.gov/images/NghiemEtAl-Movie1.avi.

that a large range of different conditions can be included in this study. The algorithm tracks the parcels by finding the maximum correlation of a 5x5 window of pixels from one day to the next until September 30, 2008, or until the parcel is "melted out" as defined by its leaving the SIE.

The tracking algorithm uses ancillary SIE products derived from passive microwave data and other satellite observations. SIE datasets are readily available from the U.S. National Ice Center (NIC) and from the Integrated Climate Data Center (ICDC). The NIC SIE mask is generated from detailed manual analyses of the extent of the sea ice cover using multiple active and passive microwave, visible, and infrared satellite data sources, including observations with spatial resolution of the order of 100 m. NIC analysts pay particular attention during their sea ice cover

127 analyses to the location of the ice edge because of the need to maintain domain awareness for
128 safe operations near the ice edge. The use of multisensory and high-resolution data provides for
129 a more accurate delineation of SIE than what could be generated alone from automated satellite
130 algorithms. The NIC sea ice edge position analyses have been validated with a good agreement
131 found by a comparison with ship observations (Ozsoy-Cicek et al., 2009). Antarctic SIE data for
132 this study are available from NIC for 2006-2009.

133 To supplement NIC SIE data product before 2006, the ICDC sea ice concentration (SIC) > 0
134 is used to determine a SIE consistent with the conservative SIE definition by NIC. ICDC SIC
135 values have been computed at the French Research Institute for Exploitation of the Sea with the
136 Arctic Radiation and Turbulence Interaction Study (ARTIST) Sea Ice algorithm (Kaleschke et
137 al., 2001; Spreen et al., 2008; Kern et al., 2010) applied to brightness temperatures measured
138 with the 85 GHz Special Sensor Microwave/Imager (SSM/I) and/or Special Sensor Microwave
139 Imager / Sounder (SSMIS) channels with a grid resolution of 12.5 km. The results have
140 compared fairly well with ship observations and with satellite products from other algorithms
141 (Beitsch et al., 2015). The combination of the NIC and ICDC SIE is used together with
142 QuikSCAT data to obtain results over the decadal period of 1999-2009.

143 Presented in Fig. 2 are the tracking points at the start on 1 June 2008 (Fig. 2a) and the
144 trajectories as these points are traced from their initial places in the austral autumn to their
145 locations on the equinox of 22 September 2008 (Fig. 2b) when the season transitioned from the
146 austral winter to the austral spring. From the trajectories, several general characteristics of
147 Antarctic sea ice dynamics are observed. There was an advection of sea ice outward and away
148 from the coast of Antarctica, especially in the Weddell, Lazarev, Riiser-Larsen, and Cosmonauts
149 Seas. Sea ice was also pushed away outward from the Ross Ice Shelf in the Ross Sea, where a

150 split in the ice drift eastward and westward could be identified (6 o'clock area on sea ice in Fig.
151 2b). In the sea ice zone behind the sea ice edge, the trajectories reveal a westward recirculation
152 of sea ice. Overall, the trajectories show that sea ice, which formed earlier around Antarctica in
153 June was forced toward lower latitudes in later months, thereby forming an outer zone of older
154 sea ice while vacating and thus diverging the internal sea ice where newer ice could grow
155 effectively.

156 A number of tracking points near the coast around Antarctica remained stationary,
157 consistently with their locations on landfast ice (multiple white areas next to the coast in Fig. 2b,
158 also see Movie 1 at http://urban.jpl.nasa.gov/images/NghiemEtAl-Movie1.avi). The capability to
159 track complex ice trajectories was verified with the existence of several icebergs that were
160 closely followed by the trajectories as found in the Cooperation Sea, where one of the icebergs
161 moved in an Ω loop (3 o'clock area in Movie 1). Specific details of the sea ice dynamics will be
162 presented together with the seasonal evolution of synoptic sea ice classes later in Section 6.

163 **4. Synoptic Patterns of Sea Ice Backscatter Signatures**

164 As indicated by the sea ice trajectory tracking, the early sea ice cover grown around the
165 Antarctic continent was forced outward toward lower latitudes to form an outer zone of sea ice
166 containing older and thus thicker and rougher sea ice with more snow accumulation, while the
167 internal ice is younger and thus thinner. From electromagnetic scattering physics based on the
168 first principle of Maxwell's equations for the snow-covered sea ice (Nghiem et al., 1990; 1993;
169 1995; Golden et al., 1998; Barber and Nghiem, 1999), the older, thicker, and rougher ice with
170 more snow must have backscatter higher than that of the younger ice.

171 From Antarctic field observations, QuikSCAT backscatter of sea ice has been shown by
172 Markus et al. (2011) to correlate with ICESat variability, which in turn correlates with the

standard deviation of the overall snow depth and ice thickness from in-situ snow and ice measurements. Toyota et al. (2011) find that the mean ice thickness of Antarctic sea ice has a correlation with surface roughness that is even higher compared to that with the mean freeboard. Thus, sea ice backscatter must be higher across the outer sea ice zone around the front of the SIE behind the ice edge to be consistent with the physical characteristics of the older sea ice in that frontal ice zone (FIZ). This needs to be investigated to verify the consistency between the patterns of sea ice age from the ice tracking results and spatial patterns of sea ice backscatter from observations with QuikSCAT satellite data.

To identify different backscatter patterns of Antarctic snow-covered sea ice, we examine its radar backscatter signatures over the Southern Ocean. Fig. 3 presents QuikSCAT backscatter synoptic images, together with multi-temporal plots along five different transects from the Antarctic coast to the ice edge as sea ice grew from June to its peak extent in September of 2008. These transects are selected to be in different regions of the Southern Ocean along these longitudes: (a) 3.38°E in the Lazarev Sea coming across Bouvet Island at 54.43°S, (b) 45.0°E in the Cosmonauts Sea, (c) 176.62°W in the Ross Sea meridionally conjugated to the Bouvet transect, (d) 135.0°W in the Amundsen Sea, and (e) 30.0°W in the Weddell Sea. Refer to Fig. 1 for geographical names.

Over the synoptic sea ice patterns and in all transects (Fig. 3), QuikSCAT satellite observations reveal a special feature of Antarctic sea ice backscatter signatures with high values (> -15 dB) forming a circumpolar band along the sea ice edge that encapsulates the internal ice pack characterized by low backscatter. Such feature is consistent with the results from ice trajectory tracking, and thereby supports the existence of the FIZ containing older sea ice that is thicker and rougher with more snow accumulation. The FIZ surrounds the internal younger sea

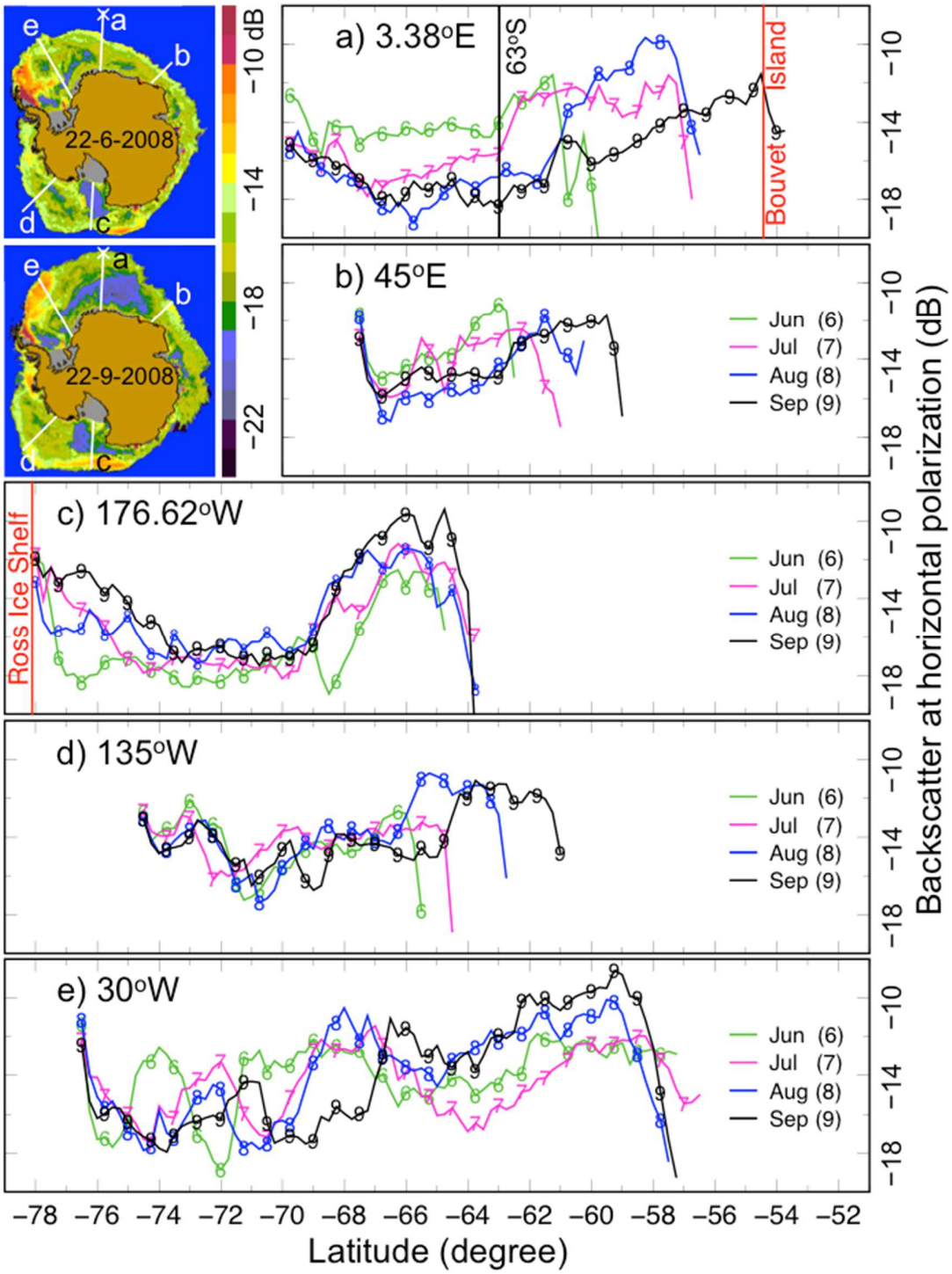

Fig. 3. Radar backscatter patterns and transect plots of Antarctic sea ice observations in 2008 by the QuikSCAT satellite scatterometer operated at the Ku-band frequency of 13.4 GHz. The top left insets are for QuikSCAT backscatter of sea ice on 22 June and 22 September 2008, where the color scale is for backscatter values, blue for ocean, grey for permanent ice, and brown for land. The backscatter plots are for (a) Transect a along 3.38°E, (b) Transect b along 45.0°E, (c) Transect c along 176.62°W, (d) Transect d along 135.0°W, and (e) Transect e along 30.0°W. The plot colors are green for June, magenta for July, blue for August, and black for September.

ice with a lower backscatter signature as much as 3-6 dB (equivalent to 2-4 times, converged into the linear domain from the logarithmic dB values) less than that of the sea ice in the FIZ (Fig. 3).

The time-series plots in Fig. 3 present the evolution of sea ice in different Antarctic regions as a function of latitude. Along Transect a (Fig. 3a) from June to July 2008, the FIZ became widened as its outer edge advanced toward Bouvet Island. In August, the FIZ inner edge was pushed outward and its width contracted. The FIZ continued extending farther north as it reached Bouvet Island in September. As an example at latitude 63°S on Transect a (vertical black line in Fig. 3a), backscatter was decreasing from June to September, indicating the northward passage of the FIZ while the space behind remained opened and even expanded for more ice divergence, thus creating new spaces where sea ice can effectively grow to form younger and thus thinner ice consistently associated with lower backscatter. If the seasonal evolution of sea ice formation were dominated only by thermodynamic ice growth in place, then the backscatter should have been increasing along with the sea ice growth at that location. This example highlights the interplay of dynamics and thermodynamics in the seasonal evolution of Antarctic sea ice.

The FIZ along Transect b (Fig. 3b), characterized by the high backscatter signature, gradually migrated northward between June and September. In the Ross Sea, it was already established by June and consistently maintained there during June-September as seen in Transect c (Fig. 3c). In the Amundsen Sea along Transect d (Fig. 3d), the FIZ moved to northward with a slight decrease in the peak magnitude between June and July then became significantly pronounced in August and September. Along Transect e (Figure 3e) in the Weddell Sea, the FIZ was the widest with the sea ice edge persisting between 57°S and 58°S. Although showing variable characteristics over different oceanic regions, these transect profiles capture the presence of the FIZ around

Antarctica constituting a circumpolar band of sea ice (GSZ), which will be quantitatively defined with synoptic sea ice classes in Section 5.

5. Synoptic Classes of Sea Ice

Here, the objective is to capture the synoptic patterns of Antarctic sea ice pertaining to different classes of sea ice having different backscatter signatures corresponding to older and younger sea ice with different ice thickness, roughness, and snow accumulation as presented earlier in Section 4. This necessitates the development of a method for a synoptic classification of Antarctic sea ice. Hence, we carry out a statistical analysis of Antarctic sea ice backscatter during the sea ice growth period from June to September over the entire Southern Ocean. We find that the backscatter histograms have a typical shape similar to that of the Gaussian distribution with a single peak. This is in contrast to the bimodal distribution of Arctic sea ice backscatter, having separate and distinctive peaks for seasonal and perennial sea ice in freezing seasons, which was used in the algorithm development for Arctic sea ice classification (Nghiem et al., 2006, Nghiem and Neumann, 2007). This is because Antarctic sea ice is dominated primarily by first-year sea ice, rather than the coexistence of two major distinctive classes of first-year (seasonal) and multi-year (perennial) ice in the Arctic (Nghiem et al., 2007).

Since the Antarctic sea ice backscatter (σ_0) statistics are similar to the Gaussian distribution, the probability density function of σ_0 is determined by two independent parameters: The mean value (σ_M) and the standard deviation (*STD*), which are used here as the basis to define synoptic sea ice classes. First, we identify the high backscatter range with values larger than σ_M as corresponding to older, rougher, and thicker sea ice with more snow in the FIZ, and the low backscatter range with values smaller than σ_M as pertaining to younger and thus thinner sea ice with less snow. Then, an additional synoptic sea ice class with backscatter larger than one *STD*

242 above σ_M is identified as corresponding to the most-deformed older ice and thus likely the
243 thickest sea ice. Based on these backscatter ranges, the following synoptic sea ice classes are
244 defined: Rough older ice (RI) for $\sigma_0 > \sigma_M + STD$, older ice (OI) for $\sigma_M + STD \geq \sigma_0 > \sigma_M$, and
245 younger ice (YI) for $\sigma_M \geq \sigma_0$. Coincidentally, these thresholds are found to be within 0.3 dB of
246 those used to identify different Arctic sea ice classes (Nghiem et al., 2006, 2007). In addition, a
247 limited amount of 'permanent' ice, including ice shelves and persistent landfast ice, is routinely
248 identified and mapped around Antarctica by the NIC (NIC, 2015).

249 Per the above definition, the synoptic sea ice classes are mapped from QuikSCAT
250 backscatter data within the ancillary SIE products from NIC and ICDC that are described earlier
251 in Section 3. Patterns of the distribution of sea ice classes are presented in Fig. 4 around the
252 September equinox in 1999-2009. This is the seasonal transition time from the austral winter
253 into the spring when the Antarctic SIE is generally at or near its maximum extent in each year.
254 In all years, the Antarctic sea ice cover was encapsulated all around the ice pack by a FIZ, which
255 is now defined as the sea ice zone consisting of RI and OI classified quantitatively with σ_M and
256 *STD* pertaining to the Gaussian statistics of sea ice σ_0. The outer ice edge of the FIZ can be
257 found close to the coast in regions such as in the Somov Sea, D'Urville Sea, and Mawson Sea, or
258 very far away from the coast particularly in the Lazarev Sea where the FIZ may extend all the
259 way to Bouvet Island (white cross in Fig. 4).

260 The FIZ characteristics around Antarctica are found to be quite variable over the years,
261 particularly in certain seas such as the Ross Sea when comparing 2001 and 2006 observations, or
262 the Weddell Sea when comparing 1999 and 2008 observations. The width at different locations
263 can vary by an order of magnitude from ~100 km to ~1000 km whereas the location of the inner

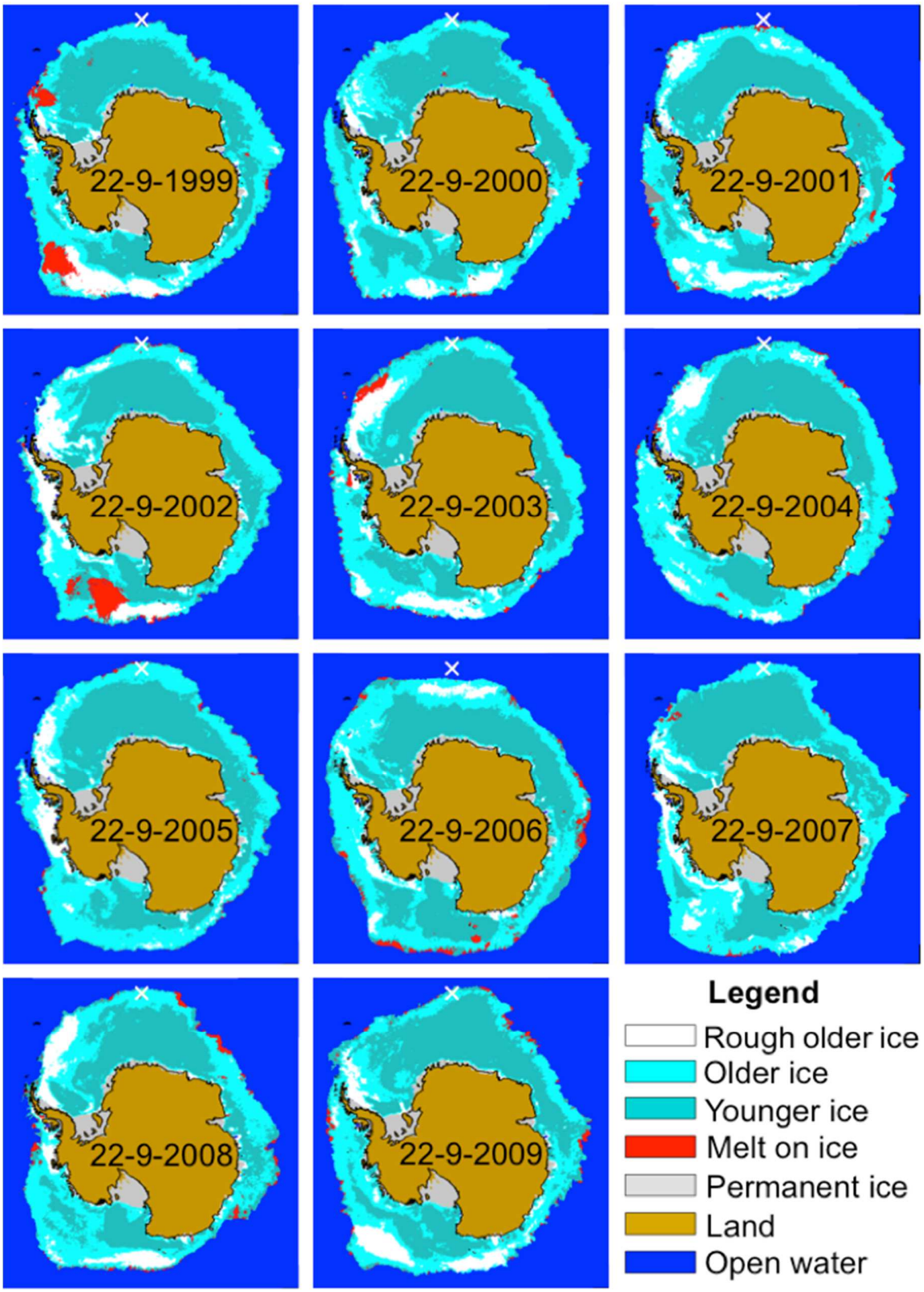

Fig. 4. Synoptic classes of Antarctic sea ice around the September equinox in 1999-2009. The location of Bouvet Island is marked with the white cross.

side of the FIZ can be very close to the Antarctic coast or more than 1000 km away. Table 1 shows quantitative examples of measurements of the FIZ widths, and the distances from its inner side to the Antarctic coast along multiple transects across various seas in the Southern Ocean at different seasonal times in 2008. Despite this large variability, the extensive circumpolar FIZ surrounds YI in the internal ice pack in all years (Fig. 4). Formed by a combination of OI and RI, it helps protect and maintain (more details later) the internal younger and thinner sea ice that likely has less snow cover due to its shorter time available for the seasonal snow accumulation. As such, the FIZ acts as a shield zone (GSZ) or a defensive barrier for the thinner and weaker internal ice pack that continues growing as the GSZ advances toward its outermost position in the austral spring as shown in the next section.

Table 1. Frontal ice zone (FIZ) distances and widths along different longitudes on 22 July, 22 August, and 22 September 2008. The FIZ distance is between the coastline (or the outer edge of Ross ice shelf) and the inner edge of FIZ. The FIZ width is between the inner and outer edges of the FIZ. The uncertainty in the FIZ distance and FIZ width is ±25 km.

Longitude (°)	Distance (km)			Width (km)		
	22 Jul	22 Aug	22 Sep	22 Jul	22 Aug	22 Sep
3.38	885	1100	1410	720	470	495
45.0	190	465	515	550	355	360
−176.62	1050	1035	1055	530	530	510

6. Seasonal Evolution of Sea Ice

To examine the seasonal evolution of sea ice, the retrieved trajectories of sea ice parcels are overlaid on maps of sea ice classes in Fig. 5 for day 22 of June, July, August, and September 2008 covering the period from around June solstice to September equinox. By 22 June 2008 (top left, Fig. 5), a sea ice cover, containing an extensive distribution of OI and RI, was observed to have formed from close to the Antarctic coast extending to the sea ice edge with areas of YI present particularly in the Weddell, Lazarev, Riiser-Larsen, Ross, and Amundsen Seas. In those

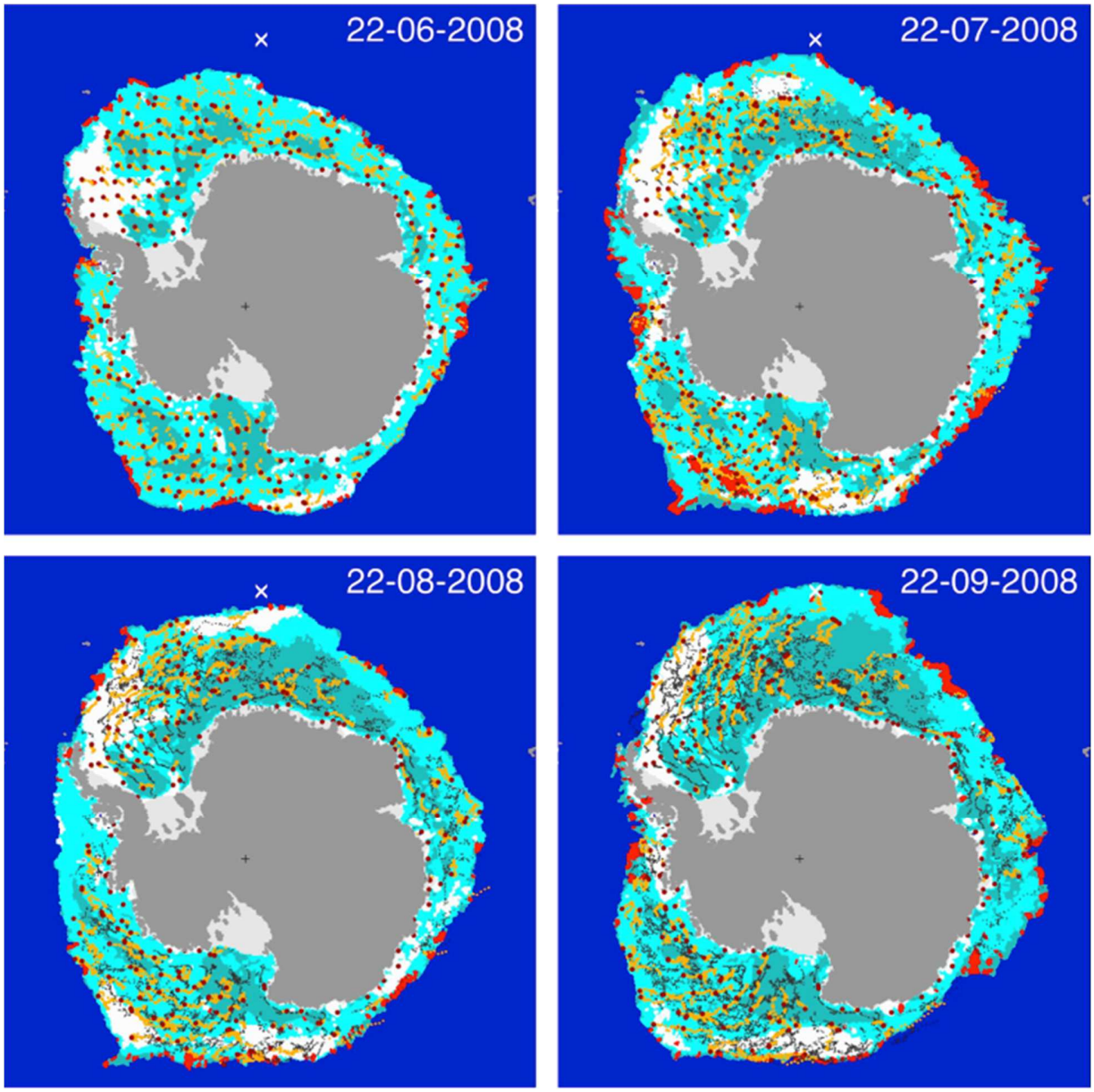

Fig. 5. Antarctic sea ice trajectories overlaid on maps of synoptic sea ice classes on 22 June, July, August, and September 2008. Red dots are the current positions of the trajectories on the given date with the orange trails indicating the drift of the tracks during the past 30 days and the trails consisting of small black dots completing all tracking points along the sea ice tracks since 1 June 2008. The color code for open water and sea ice classification is the same as in Figure 4. Dark grey represents land. The location of Bouvet Island is marked with the white cross.

287 seas, the older sea ice moved outward, driven by katabatic winds that created open space behind
288 the FIZ for YI to grow (see Movie 1). However, the sea ice edge was the closest to the Antarctic
289 coastline in the D'Urville Sea to Mawson Sea region.

By 22 July (top right, Fig. 5), the FIZ advanced farther north in the South Atlantic toward Bouvet Island with the internal YI expanding to a larger region behind a more distinctive FIZ from the Weddell Sea through the Lazarev Sea to the Riiser-Larsen Sea. Sea ice trajectories adjacent to the coast along the Lazarev and Riiser-Larsen Seas showed a westward drift driven by the polar easterlies. As sea ice moved outward in the Weddell and Lazarev Seas, the ice trajectories curved eastward as driven by the westerlies. In the Ross Sea, the sea ice edge could only reach slightly northward while the region of YI in the internal ice pack was maintained by sustaining winds off the Ross Ice Shelf. In this region, sea ice trajectories revealed a split eastward and westward as sea ice moved outward away from the shoreline (Movie 1). From the D'Urville Sea to Mawson Sea, the ice edge was stable and did not extend much farther after June with some motions corresponding to the easterlies along the coast. Several small areas of transient ice surface melt occurred along the ice edge and within FIZ (top right, Fig. 5).

By August (lower left panel, Fig. 5), the region of internal YI in the Weddell Sea through Lazarev Sea to Riiser-Larsen Sea had grown larger. The inner side of the FIZ was also pushed outward while the outer side had not advanced or even slightly retreated in the Weddell Sea, resulting in a smaller FIZ width. Sea ice trajectories tracked from June to August clearly show the cyclonic pattern of the Weddell Gyre formed by the Antarctic Circumpolar Current (ACC) interactions with the Antarctic Continental Shelf. The internal YI also appeared larger in Cooperation Sea behind the FIZ. In the Ross Sea, the internal YI was persistent while sea ice trajectories off the Ross Ice Shelf exhibited the westward and eastward split (also see Movie 1). The pattern of the Ross Sea gyre became well defined by the long June-August trajectories of sea ice as the outer OI and RI arched and followed along the westerlies (Movie 1). Again sea ice in

312 the D'Urville Sea to the Mawson Sea region remained stable, although with transient melt areas
313 occurred on the sea ice surface near the ice edge.

314 By September (lower right, Fig. 5), the internal YI extent became the largest as the inner side
315 of the FIZ advanced northward across the Weddell, Lazarev, Riiser-Larsen, and Cosmonaut
316 Seas, while the trajectories of OI and RI in the FIZ traced along consistently with the westerlies.
317 At this time, the outer side of the FIZ reached Bouvet Island. In the Ross Sea, the internal YI
318 extent became larger compared to that in earlier months while the outer sea ice in the FIZ
319 continued to be entrained by the westerlies (Movie 1). The extent of the internal YI in the
320 Cooperation and Davis Seas also widened. The sea ice edge retreated in the D'Urville Sea while
321 it extended in the adjacent Mawson Sea. Between June and September, SIE in the
322 Bellingshausen Sea was variable with intermittent retreats and advances while transient melt
323 areas on the sea ice surface were observed in different months (Fig. 5). In late September, the
324 FIZ was still persistently surrounding and protecting the internal sea ice around Antarctica while
325 sea ice in the FIZ was consistently recirculated by the westerlies (Movie 1). In an opposite
326 manner, winds in the Arctic can significantly contribute to sea ice loss such as the 'Polar
327 Express' driven by the dipole pattern of atmospheric anomalies (Nghiem et al., 2007; Perovich et
328 al., 2011), which accelerates sea ice transport directly out of Fram Strait in the Arctic.

329 **7. Factors Influencing the Formation and Evolution of Sea Ice**

330 Given the new insights derived from the above observations of sea ice trajectories and
331 synoptic classes, next we discuss factors that enhance the growth and persistently maintain the
332 Antarctic sea ice cover. First, regarding the physical characteristics of sea ice itself, the FIZ
333 consisting of older and thicker sea ice with more snow accumulation adjacent to the sea ice edge
334 constitutes an opposite condition to what is typically found in the Arctic where the peripheral

335 marginal ice zone (MIZ) mostly consists of younger, thinner, and smoother level first-year sea
336 ice with less snow (except in Greenland Sea) including unconsolidated pancake, nilas, and new
337 ice like frazil and grease ice (WMO, 2014), easily broken up by wind-wave actions and melted
338 from surface by warm air or from beneath by warm waters (Perovich et al., 2015, Webster et al.,
339 2014, 2015) and sensitive to dynamic or thermodynamic forcing that reduces sea ice in the Arctic
340 (Perovich, 2011). Moreover, the older and thicker sea ice in the Antarctic FIZ, extending 100 km
341 to 1000 km (Section 5) around the ice pack, can suppress sea states more effectively and thus
342 reduce sea ice break-up induced by storms as compared to feeble ice conditions in the Arctic
343 MIZ.

344 In the internal sea ice region behind the FIZ, persistent katabatic winds force the opening,
345 production, and advection of ice. In the newly opened or ice divergence areas, protected behind
346 the FIZ, the YI can have a large growth rate, inversely related to sea ice thickness by as much as
347 an order of magnitude between thin and thick ice (Thorndike et al., 1975). Sea ice production is
348 thus enhanced as winds keep refreshing the effective growth of the pack with fast-growing new
349 ice (Heil et al., 1998). In leads and polynyas opened by persistent winds, ice production is so
350 effective that these areas are considered as ice factories (Barber and Massom, 2007), which
351 amply supply sea ice and thus contribute to sustaining the Antarctic sea ice cover. As the internal
352 ice is forced to converge toward the inner side of the formidable FIZ, ice ridging is enhanced and
353 ice volume can increase dynamically by ice convergence as suggested by Zhang (2013). Field
354 observations in the Bellingshausen and Amundsen Seas indicate that rafting and ridging play
355 important roles at different stages of sea ice floe development in the process of floe thickening
356 (Worby et al., 1996).

357 The general pattern of persistent offshore winds that drive the FIZ outward (Movie 1) is also
358 effective in promoting sea ice growth by the advection of very cold air to grow more ice, by the
359 forcing to advance the sea ice edge outward, and by the suppression of waves due to the ice
360 advancing and thus impeding water mixing and subsurface melt (Nghiem et al., 2012). Offshore
361 winds blowing across the sea ice surface are also less effective in creating large waves, and thus
362 resulting a calm sea state (Nghiem et al., 2012). When on-ice winds occur, sea ice near the edge
363 can become compacted (Massom et al., 2008), thereby reinforcing the FIZ. Furthermore, such
364 compaction promotes the jet formation (Heorton et al., 2014) that sustains the recirculation of sea
365 ice in the FIZ.

366 Winds such as the polar westerlies, easterlies, and offshore katabatic winds play a major role
367 in forcing sea ice growth and dynamics as presented above. The pattern of wind fields around
368 Antarctica is consistently controlled and shaped by the Antarctic topography, including the
369 coastal morphology and the presence of the ice sheet and associated ice shelves. Parish and
370 Cassano (2003) found that Antarctic surface winds display a high degree of persistence with
371 mean directions related to the local topographic configuration of the ice sheet. In their flow
372 simulation, the initial arbitrary circumpolar low-level winds become modified by the Antarctic
373 terrain within 72 hours such that the direction of the wind vectors becomes tied to the underlying
374 terrain. Results from this simulation and from later analyses (Parish et al., 2006) even hint at the
375 westward and eastward split off the Ross Ice Shelf, which is evident in sea ice drift trajectories
376 observed with satellite data (see the region of sea ice at 6 o'clock in Movie 1). Parish and
377 Cassano (2003) further suggest that the establishment of the low-level wintertime Antarctic wind
378 field is critically dependent on the role of topography in shaping the Antarctic boundary layer
379 winds through blocking and subsequent adjustment.

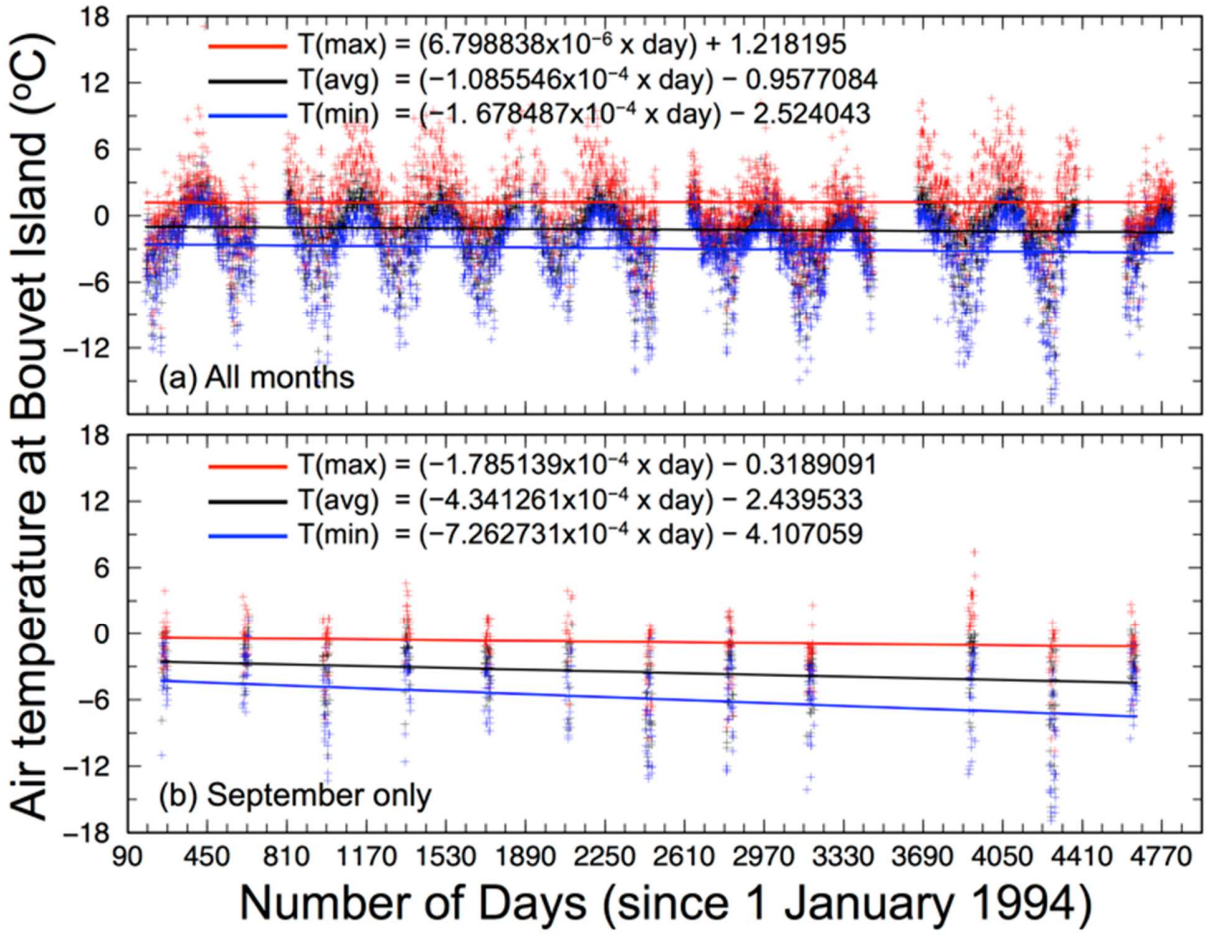

Fig. 6. Air temperature measured at Bouvet Island, obtained from the National Oceanic and Atmospheric Administration (NOAA) Global Surface Summary of the Day (GSOD) dataset (https://data.noaa.gov/dataset/global-surface-summary-of-the-day-gsod). The horizontal axis is for number of days counted from 1 January 1994 (1 is for 1 January 1994, 366 is for 1 January 1995, etc.). This uninhabited island is located near a triple junction on the southern end of the Mid-Atlantic Ridge. It is the most remote island in the world with more than 1,600 km away from the nearest land in any direction.

During the growth season, Antarctic sea ice reaches north up to an oceanic frontal zone, where SIE cannot advance much farther and seems to be constrained to certain locations in various regions of the Southern Ocean (Movie 1). Throughout the decade of 1999-2009, the SIE attained its maxima at or near Bouvet Island around the September equinox (Fig. 4), except in 2001 and 2006 when SIE also expanded to the island but later in October. Over an extensive region in the Southern Ocean from north of Bouvet Island to the Antarctic coast, more than 11,000 conductivity-temperature-depth profiles, collected by sensors mounted on southern

388 elephant seals in February-November 2008, showed a water mass transition from the warm ACC
389 Regime to the Weddell Cold Regime across Bouvet Island (Biuw et al., 2010; Zhou, 2013). This
390 oceanic frontal pattern of warm and cold waters, spanning across Bouvet Island, continues
391 delimiting the northern extent of the Antarctic sea ice cover in the South Atlantic Ocean, as sea
392 ice cannot survive when it reaches the warm waters. Moreover, air temperatures measured at
393 Bouvet Island have been stable over a period of 13 years since 1994 (Fig. 6), which is another
394 factor supporting the sea ice stability in this region.

395 To examine patterns of SST around SIE, the Multi-sensor Ultra-high Resolution (MUR) SST
396 product was obtained from the Physical Oceanography Distributed Active Archive Center
397 (MUR, 2010), which has a relative accuracy of 0.5°C in high-latitude oceans. As examples,
398 MUR SST for 2008 and 2009 are overlaid on SIE around September equinox (Fig. 7). The
399 results reveal that SIE closely conforms to the isotherm at −1.4°C, slightly above a seawater

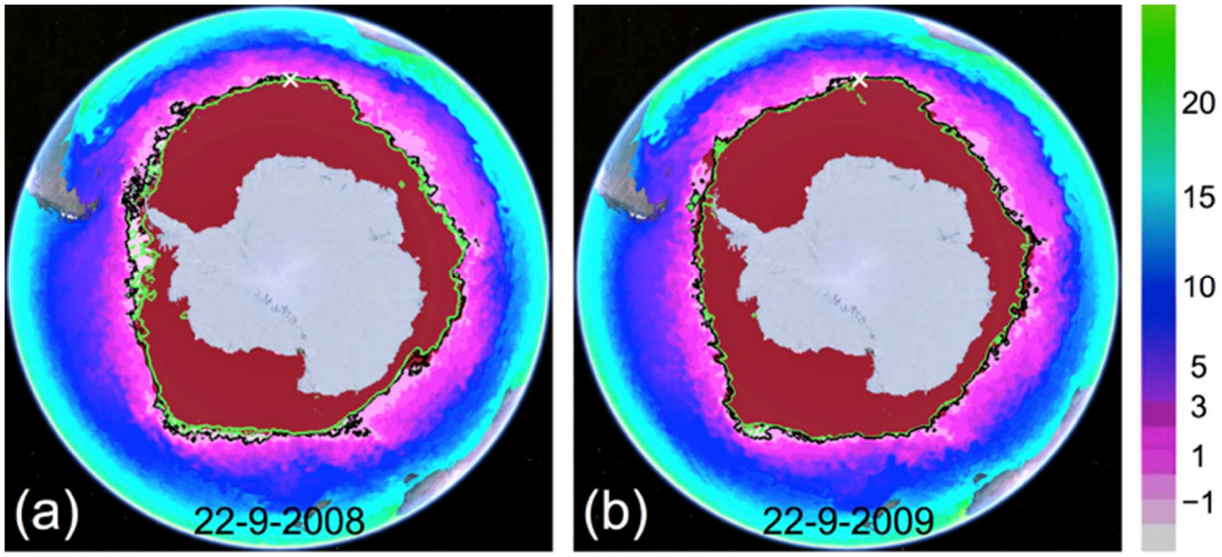

Fig. 7. Maps of Multi-sensor Ultra-high Resolution (MUR) Sea Surface Temperature (SST) represented by the color bar in degrees Celsius on the right with isotherms at −1.0°C (black contour) and −1.4°C (green contour) on National Ice Center (NIC) Sea Ice Extent (SIE) mask in maroon for: (a) 22 September 2008, and (b) 22 September 2009. The white cross marks the location of Bouvet Island.

400 freezing point around −1.9°C (Foldvik and Kvinge, 1974). The SST isotherm at −1.0°C is also
401 relatively close to the ice edge in most places, although it may have some detachment from the
402 SIE in some cases such as in the Bellingshausen Sea in 2008 (Fig. 7). In general, the SIE is
403 typically enclosed by the −1.0°C SST isotherm in each year.

404 The overall conformance of SIE to the SST isotherms indicate that ocean temperatures exert
405 significant control in delimiting the maximum reach of SIE. In turn, patterns of warm and cold
406 waters associated with oceanic fronts are significantly governed by bathymetry (Orsi et al., 1995;
407 Moore et al., 1997; Langlais et al., 2011; Kim and Orsi, 2014). In particular, Kim and Orsi used
408 buoy, hydrographic, and altimetric data to infer ACC fronts and their variability between 1992-
409 2011, which encompasses the entire period (1999-2009) considered in this study.

410 In the Southern Ocean, the locations of −1.0°C SST isotherms on 22 September in 1999-2009
411 are closely bundled, especially around the region of Bouvet Island and the meridionally
412 conjugate region (180° away in longitude) on the opposite side of the continent (Fig. 8). These
413 isotherms are in the proximity of the southern ACC front, or sACCf, delineated by Kim and Orsi
414 (2014) (Fig. 8) and by others (Orsi et al., 1995; Sokolov and Rintoul, 2009). Pronounced
415 seafloor features can strongly guide sACCf, such as in the region around Bouvet Island, located
416 at a triple junction of the American-Antarctic, Mid-Atlantic, and Atlantic-Indian Ridges, and in
417 the region of Pacific-Antarctic Ridge in the Somov Sea.

418 Notably, the −1.0°C SST isotherms cut across the Kerguelen Plateau (Fig. 9) through the
419 Fawn Trough where sACCf transports in conformity with the bathymetry (Park et al., 2009).
420 This is also where the seasonal maximum SIE can recurrently reach to, but cannot cross over to
421 the warm side. While effects of Antarctic bathymetry may contribute to the overall stability of

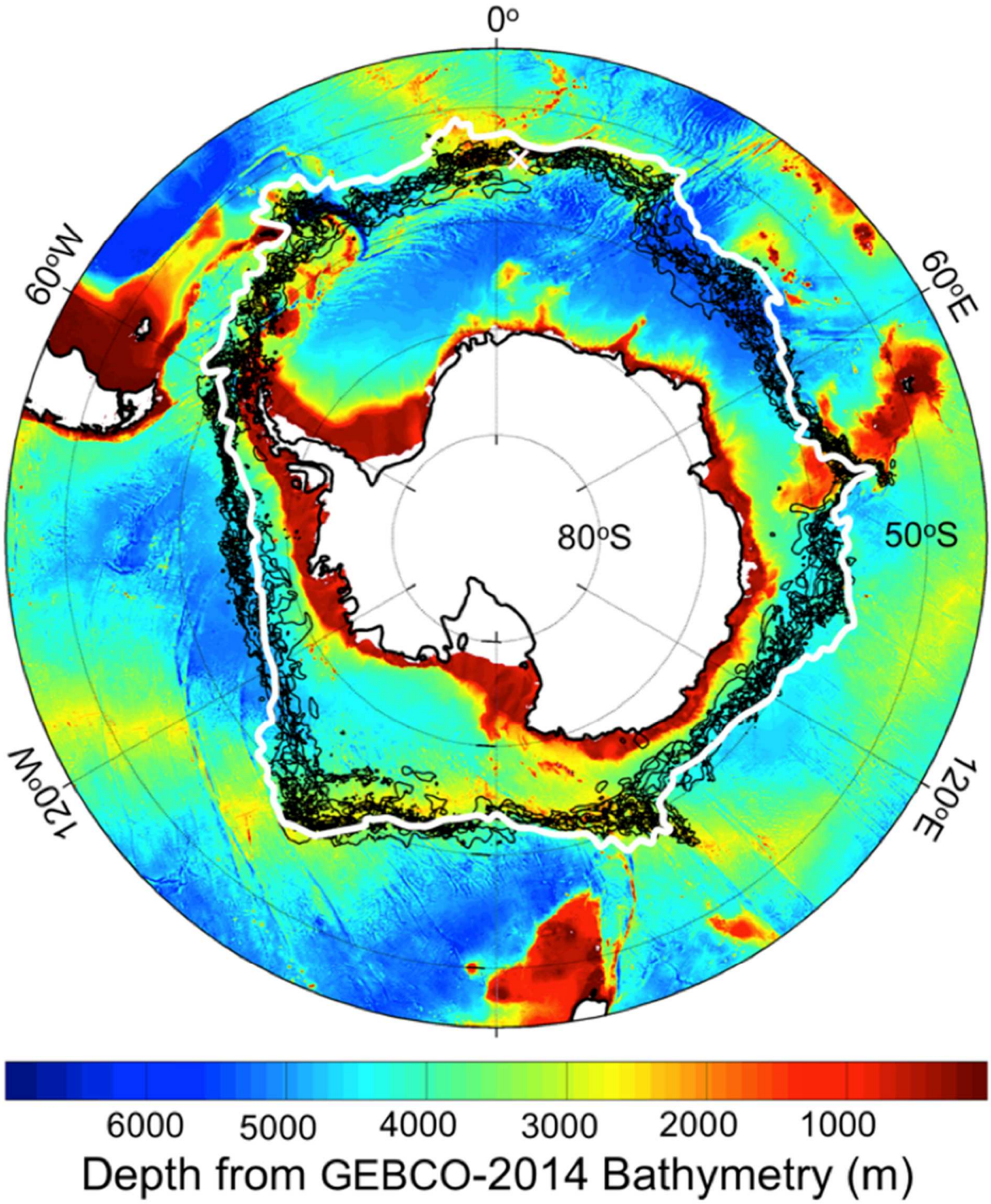

Fig. 8. Map of the southern Antarctic Circumpolar Current (ACC) front (sACCf) delineated by the white contour (Kim and Orsi, 2014) with MUR SST −1.0°C isotherms represented by the black contours on 22 September in 2002-2009 plotted together with the GEBCO-2014 bathymetry. The isotherms are closely bundled close to the sACCf over pronounced seafloor features such as ridges while they tend to spread apart across smooth abyssal plains. The white cross marks the location of Bouvet Island.

422

423 Antarctic sea ice, bathymetry in the Arctic in contrast may work to reduce sea ice more
424 effectively. For example, the landfast sea ice recurrently controlled by the seafloor across the
425 mouth of the Mackenzie River may delay the river discharge to accumulate a larger volume of
426 warmer waters later breaking through the landfast ice to melt more sea ice (Nghiem et al., 2014).
427 Climate-ocean models also indicate that oceanic fronts are tightly constrained by the local

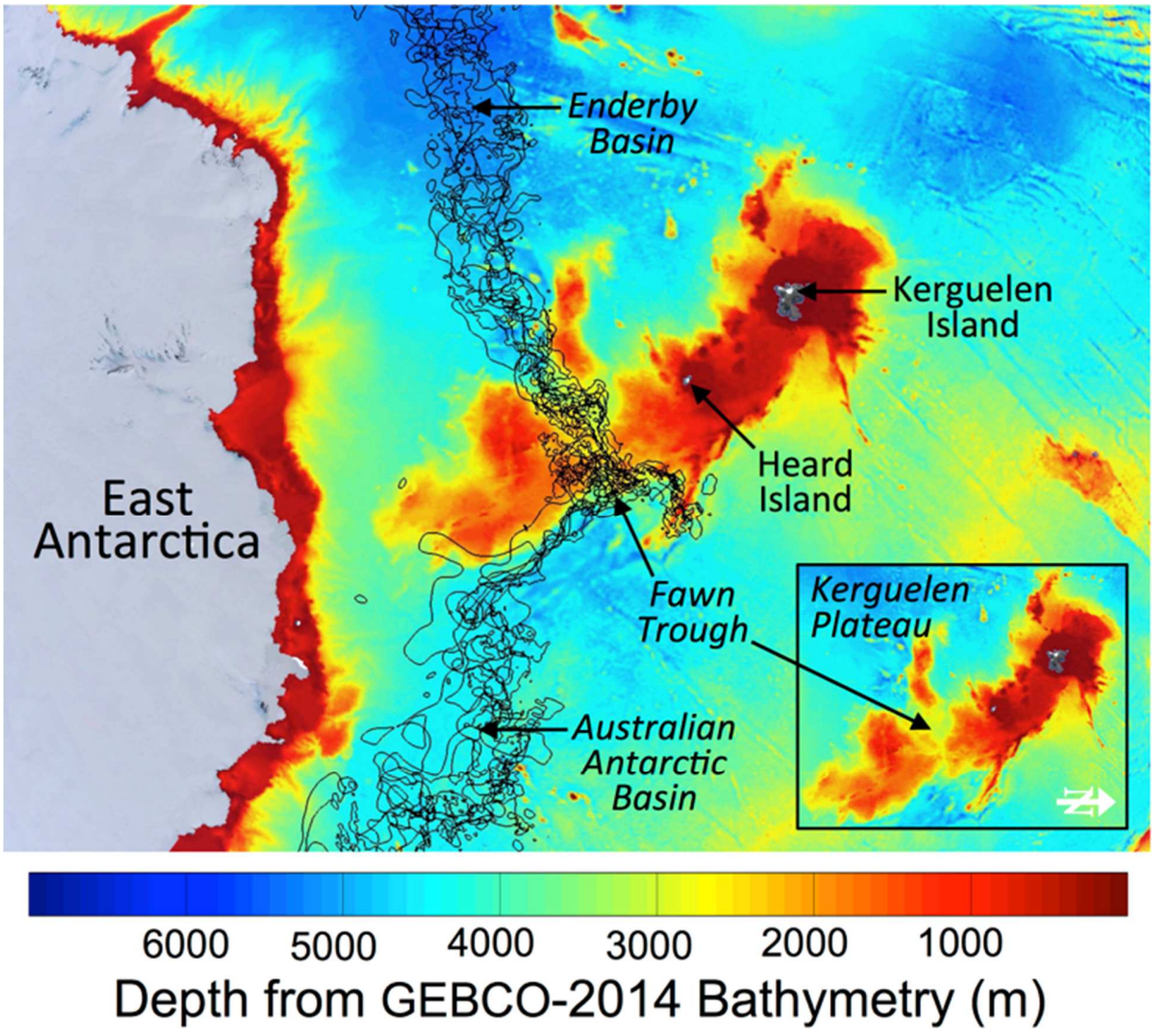

Fig. 9. Map of MUR SST –1.0°C isotherms as black contours on 22 September in 2002-2009 on the GEBCO-2014 bathymetry in the region of the Kerguelen Plateau, a submerged microcontinent. The isotherms closely bundle as they pass across the Kerguelen Plateau through the Fawn Trough. However, the isotherms tend to spread apart over the deep Enderby Basin and the deep Australian Antarctic Basin where seafloor features are not pronounced.

bathymetry (Graham et al., 2012; de Boer et al., 2013), while Coupled Model Intercomparison Project phase 5 (CMIP5) simulations report no significant relationship between the latitudinal positions of the ACC fronts and the westerlies (Meijers et al., 2012). However, the bathymetry may impose less control on the sACCf over the abyssal plains and in deep basins, thereby allowing more effects from atmospheric drivers like SAM and El Niño Southern Oscillation (Kim and Orsi, 2014). These dynamic atmospheric effects can cause more sea ice variability, particularly over the Bellingshausen Plain that is a deep basin (Fig. 8, also see Fig. 1 for the location of the Bellingshausen Plain). The different levels of bathymetry control on SST are also observed over the Kerguelen Plateau, a submerged microcontinent (Fig. 9) also called by paleogeologists and geographers as a submerged continent (Edmond, 2013; World Heritage Encyclopedia, 2016), as the MUR SST isotherms closely pinch through Fawn Trough while they tend to expand over the abyssal plains in the Enderby and Australian Antarctic Basins.

In summary, the stark contrast in geophysical characteristics between the southern and northern polar regions causes different behaviors of Antarctic and Arctic sea ice. Regarding sea ice properties, the Antarctic circumpolar FIZ with older rougher and thicker sea ice acts a Great Shield to protect the younger internal ice, as opposed to the Arctic MIZ with younger and thinner sea ice that is easily broken up and melted away. Regarding atmospheric forcing, persistent Antarctic winds create ice factories, thicken ice by ridging, and recirculate ice to enhance and sustain the sea ice cover, as opposed to Arctic winds contributing to sea ice loss such as the 'Polar Express' that efficiently exports sea ice directly to warm ocean where it melts. Regarding oceanic effects, the Antarctic bathymetry guides the distribution of water masses to constrain the location of the sACCf that holds the persistence of the sea ice cover, as opposed the Arctic

450 bathymetry responsible for mechanisms that aggravate sea ice loss (e.g., release of warm waters
451 from the Mackenzie River).

452 **8. Conclusion and Discussions**

453 Based on daily observations acquired by the SeaWinds scatterometer aboard QuikSCAT
454 from 1999-2009, we have tracked sea ice trajectories and mapped synoptic sea ice classes (RI,
455 OI, and YI) around Antarctica. Trajectories of sea ice tracked in the 2008 growth season (June-
456 September) illustrate the pattern of Antarctic sea ice growth and dynamics, showing the outward
457 expansion of the FIZ where OI and RI accrues and recirculates along with the polar westerlies.
458 Persistent offshore winds recurrently open internal space for effective ice production behind the
459 extensive FIZ, which serves as the GSZ that in turn protects the internal YI. These mechanisms
460 can enhance sea ice production with a high growth rate in the internal YI together with rafting
461 and ridging behind the FIZ that protects and thus persistently preserves the seasonal sea ice pack
462 in the Southern Ocean.

463 As the Antarctic sea ice cover is sustained under the influence of winds guided by
464 topography and waters guided by bathymetry, the general stability of Antarctic sea ice is
465 maintained by both topographic and bathymetric characteristics as these are stable geological
466 factors. Nevertheless, a large regional variability of the SIE can still occur such as in the
467 Bellingshausen Sea where sea ice can advance, retreat, or melt intermittently because the deep
468 abyssal plain does not exert a strong control on water masses and thus allow variable effects
469 from atmospheric forcing. The thermodynamic and dynamic interplay in the Antarctic sea ice
470 formation and evolution processes is consistent with the regional geophysical characteristics that
471 are in a stark contrast to those in the Arctic, thus the different behaviors of sea ice observed in
472 the polar regions should not be considered a paradox.

While the synoptic sea ice classes defined in this study use statistics of sea ice backscatter, the specific ranges of physical properties pertaining to various sea ice classes still need to be further determined from multiple satellite active and passive sensors together with field observations (e.g., International Polar Year Antarctic Sea Ice Processes and Climate (ASPeCt) at http://aspect.antarctica.gov.au/ipy), and must be rigorously connected with physical-based scattering and emission physics from the first principles founded by Maxwell's equations. Patterns of sea ice classes and their characteristics and thickness are necessary to assess ice volume in the FIZ and over the ice production regions behind it, using remote sensing (e.g., interferometry and altimetry) and in-situ networks (e.g., International Programme for Antarctic Buoys at http://www.ipab.aq/). Moreover, autonomous sensors in submerged vehicles (e.g., Williams et al., 2014) or on drones can avoid thickness bias. This is because surveys by such sensors are not limited to selective thinner ice conditions, usually sought after as accessible routes during icebreaker operations.

Satellite data and field observations have been acquired at different times, in different seasons and years, and over different regions of Southern Ocean. However, a well designed mission using aircraft and/or satellite remote sensing in conjunction with surface networks and coordinated field campaigns is still necessary to characterize the FIZ. Such a study needs to include the internal ice production processes and their seasonal evolution in order to quantitatively capture the dynamic and thermodynamic processes at play, and thereby rigorously examine the specific regional behaviors of Antarctic sea ice. More complete and accurate datasets also become available for key parameters such as bathymetry (Weatherall et al., 2015) and topography (Zink and Moirera, 2015). These can help advance the understanding and thus improve models that resolve inconsistencies with observations to capture the true Antarctic sea

ice behavior in sea ice modeling. With these considerations, advanced research remains necessary to explain not only present behavior, but also to be able to forecast the response of the Antarctic sea ice cover to climate change given the geophysical constraints described in this paper.

Acknowledgments

The research carried out at the Jet Propulsion Laboratory, California Institute of Technology, was supported by the National Aeronautics and Space Administration (NASA) Cryospheric Sciences Program. This research was also carried out in part under the support of the National Oceanic and Atmospheric Administration (NOAA) via a subcontract to the Joint Institute for Regional Earth System Science and Engineering of the University of California at Los Angeles. Rigor is funded by NASA, National Science Foundation, and NOAA. The statements, findings, conclusions, and recommendations in this paper are those of the authors and do not necessarily reflect the views of NOAA or the Department of Commerce. We thank S. Helfrich of NIC for preparing NIC SIE data, L. Kaleschke of the University of Hamburg for helping in the ICDC SIE data access, D. T. Nguyen of JPL for assisting in GEBCO bathymetry representation, and J. Vazquez and T. M. Chin of JPL for the MUR SST data access and documentation. We thank the reviewers, all having positive and constructive comments and suggestions in the review process by Remote Sensing of Environment. In particular, we highly appreciate the excellent and thorough review by Claire Parkinson of the NASA Goddard Space Flight Center.

Data sources

Data can be found at https://podaac.jpl.nasa.gov/ for QuikSCAT, http://dx.doi.org/10.5067/GHGMR-4FJ01 for sea surface temperature, http://www.natice.noaa.gov/Main_Products.htm for NIC sea ice products,

519 http://www.gebco.net/data_and_products/gridded_bathymetry_data/ for GEBCO 2014
520 bathymetry, and https://data.noaa.gov/dataset/global-surface-summary-of-the-day-gsod for air
521 temperature data.

522 **References**

523 Ackley, S. F., & Sullivan, C. W. (1994). Physical controls on the development and
524 characteristics of Antarctic sea-ice biological communities: A review and synthesis. *Deep*
525 *Sea Research Part 1*, *41*, 1583-1604, doi:10.1016/0967-0637(94)90062-0.

526 Barber, D. G., & Nghiem, S. V. (1999). The Role of Snow on the Thermal Dependence of
527 Microwave Backscatter over Sea Ice. *J. Geophys. Res*., 104(C11), 25789-25803.

528 Barber, D. G., & Massom, R. A. (2007). The role of sea ice in Arctic and Antarctic polynyas. Ch.
529 1, pp. 1-54, in *Polynyas: Windows to the World*, eds. W. O. Smith, Jr. and D. G. Barber,
530 Elsevier Oceanography Series 74, Elsevier, Amsterdam, the Netherlands.

531 Beitsch, A., Kern, S., & Kaleschke, L. (2015). Comparison of SSM/I and AMSR-E sea ice
532 concentrations with ASPeCt ship observations around Antarctica. *IEEE Trans. Geosci.*
533 *Remote Sens*., *53*(4), 1985-1996, doi:10.1109/TGRS.2014.2351497.

534 Bintanja, R., van Oldenborgh, G. J., Drijfhout, S. S., Wouters, B., & Katsman, C. A. (2013).
535 Important role for ocean warming and increased ice-shelf melt in Antarctic sea-ice
536 expansion. *Nature Geosci*., *6*(5), 376-379, doi:10.1038/NGEO1767.

537 Biuw, M. et al. (2010). Effects of Hydrographic Variability on the Spatial, Seasonal and Diel
538 Diving Patterns of Southern Elephant Seals in the Eastern Weddell Sea. *PLoS ONE*, *5*(11),
539 e13816, doi:10.1371/journal.pone.0013816.

540 de Boer, A. M., Graham, R. M., Thomas, M. D., & Kohfeld, K. E. (2013). The control of the
541 Southern Hemisphere westerlies on the position of the Subtropical Front. *J. Geophys. Res.*,
542 *118*, 5669–5675, doi:10.1002/jgrc.20407.

543 Edmond, M. (2013), *Zone of the Marvellous: In Search of the Antipodes*, 242 pp., Auckland
544 University Press, New Zealand.
545 Foldvik, A., & Kvinge, T. (1974). Conditional instability of sea water at the freezing point.
546 *Deep-Sea Res*., *21*, 169-174, doi:10.1016/0011-7471(74)90056-4.
547 Gagné, M.-È., Gillett, N. P., & Fyfe, J. C. (2015). Observed and simulated changes in Antarctic
548 sea ice extent over the past 50 years. *Geophys. Res. Lett*., *4*2, 90-95,
549 doi:10.1002/2014GL062231.
550 Gillett, N. P., & Thompson, D. W. J. (2003). Simulation of recent Southern Hemisphere climate
551 change. *Science*, 302(5643), 273–275.
552 Golden, K. M., Cheney, M., Ding, K. H., Fung, A. K., Grenfell, T. C., Isaacson, D., Kong, J. A.,
553 Nghiem, S. V., Sylvester, J., & Winebrenner, D. P. (1998). Forward Electromagnetic
554 Scattering Models for Sea Ice. *IEEE Trans. Geosci. Remote Sens*., 36(5), 1655-1674.
555 Graham, R. M., Heywood, K. J., Chapman, M. R., & Stevens, D. P. (2012). Southern Ocean
556 fronts: Controlled by wind or topography? *J. Geophys. Res*., *117*, C08018,
557 doi:10.1029/2012JC007887.
558 Heil, P., Lytle, V. I, & Allison, I. (1998). Enhanced thermodynamic ice growth by sea-ice
559 deformation. *Ann. Glaciol*., Ed. Budd, W. F., 27, 433-437.
560 Heorton, H. D. B. S., Feltham, D. L., & Hunt, J. R. C. (2014). The Response of the Sea Ice Edge
561 to Atmospheric and Oceanic Jet Formation. *J. Phys. Oceanogr*., *44*, 2292-2316,
562 doi:10.1175/JPO-D-13-0184.1.
563 Holland, P. R. (2014). The seasonality of Antarctic sea ice trends. *Geophys. Res. Lett*., *41*, 4230-
564 4237, doi:10.1002/2014GL060172.

565 IPCC (2013). *Climate Change 2013: The Physical Science Basis*. Contribution of Working
566 Group I to the Fifth Assessment Report of the Intergovernmental Panel on Climate Change
567 [Stocker and 9 others (eds.)]. Cambridge University Press, Cambridge, United Kingdom and
568 New York, NY, USA, 1535 pp.
569 Jeffries, M. O., Worby, A. P., Morris, K., & Weeks, W. F. (1997). Seasonal variations in the
570 properties and structural composition of sea ice and snow cover in the Bellingshausen and
571 Amundsen seas, Antarctica. *J. Glac*., *43*(143), 138-151.
572 Kaleschke, L., et al. (2001). SSM/I sea ice remote sensing for mesoscale ocean-atmosphere
573 interaction analysis. *Can. J. Remote Sens*., *27*(5), 526–537.
574 Kern, S., Kaleschke, L., & Spreen, G. (2010). Climatology of the Nordic (Irminger, Greenland,
575 Barents, Kara and White/Pechora) Seas ice cover based on 85 GHz satellite microwave
576 radiometry: 1992–2008. *Tellus*, 62A, 411-434, doi:10.1111/j.1600-0870.2010.00457.x.
577 Kern, S., & Spreen, G. (2015). Uncertainties in Antarctic sea-ice thickness retrieval from ICESat.
578 *Ann. Glaciol.*, *56*(69), 107-119, doi:10.3189/2015AoG69A736.
579 Kim, Y. S., & Orsi, A. H. (2014). On the Variability of Antarctic Circumpolar Current Fronts
580 Inferred from 1992–2011 Altimetry. *J. Phys. Oceanogr*., *44*, 3054-3071, doi:10.1175/JPO-D-
581 13-0217.1.
582 Kurtz, N. T., & Markus, T. (2012). Satellite observations of Antarctic sea ice thickness and
583 volume. *J. Geophys. Res*., *117*, C08025, doi:10.1029/2012JC008141.
584 Langlais, C., Rintoul, S., & Schiller, A. (2011). Variability and mesoscale activity of the
585 Southern Ocean fronts: Identification of a circumpolar coordinate system, *Ocean Modelling*.
586 *39*, 79-96, doi:10.1016/j.ocemod.2011.04.010.

587 Lewis, M. J., Tison, J. L., Weissling, B., Delille, B., Ackley, S. F., Brabant, F., & Xie, H.,
588 (2011). Sea ice and snow cover characteristics during the winter-spring transition in the
589 Bellingshausen Sea: An overview of SIMBA 2007. *Deep-Sea Res. II*, *58*(9-10), 1019-1038,
590 doi:10.1016/j.dsr2.2010.10.027.
591 Maksym, T., Stammerjohn, S. E., Ackley, S., & Massom, R. (2012). Antarctic Sea Ice – A Polar
592 Opposite? *Oceanography, 25*(3), 140–151, doi:10.5670/oceanog.2012.88.
593 Manabe, S., Stouffer, R. J., Spelman, M. J., & Bryan, K. (1991). Transient Responses of a
594 Coupled Ocean-Atmosphere Model to Gradual Change of Atmospheric CO2. Part I: Annual
595 Mean Response. *J. Clim.*, *4*, 785-818.
596 Markus, T., Massom, R., Worby, A., Lytle, V., Kurtz, N., & Maksym, T. (2011). Freeboard,
597 snow depth and sea-ice roughness in East Antarctica from in situ and multiple satellite data.
598 *Ann. Glaciol.*, *52*(57), 242-248.
599 Marshall, G. J. (2003). Trends in the Southern Annular Mode from Observations and Reanalyses.
600 *J. Clim.*, 16, 4134-4143.
601 Massom, R. A., et al. (2001). Snow on Antarctic sea ice. *Review of Geophysics*, *39*(3), 413-445,
602 doi:10.1029/2000RG000085.
603 Massom, R. A., et al. (2008). West Antarctic Peninsula sea ice in 2005: Extreme ice compaction
604 and ice edge retreat due to strong anomaly with respect to climate. *J. Geophys. Res.*, *113*,
605 C02S20, doi:10.1029/2007JC004239.
606 Massom, R. A., Reid, P., Stammerjohn, S., & Barreira, S. (2009). Sea ice extent and
607 concentration, Antarctica. Chapter 6 in "State of the Climate in 2008," *Bull. Amer. Meteor.*
608 *Soc.*, *90*(8), S1–S196.

609 Meijers, A. J. S., Shuckburgh, E., Bruneau, N., Sallée, J.-B., Bracegirdle, T. J., & Wang, Z.
610 (2012). Representation of the Antarctic Circumpolar Current in the CMIP5 climate models
611 and future changes under warming scenarios. *J. Geophys. Res.*, *117*, C12008,
612 doi:10.1029/2012JC008412.
613 Moore, J. K., Abbott, M. R., & Richman, J. G. (1997). Variability in the location of the Antarctic
614 Polar Front (90º-20ºW) from satellite sea surface temperature data. *J. Geophys. Res.*,
615 *102*(C13), 27825-27833.
616 MUR (2010), JPL MUR MEaSUREs Project, GHRSST Level 4 MUR Global Foundation Sea
617 Surface Temperature Analysis. Ver. 2. PO.DAAC, CA, USA, available at
618 http://dx.doi.org/10.5067/GHGMR-4FJ01, accessed 12 February 2015.
619 Nghiem, S. V., Borgeaud, M., Kong, J. A., & Shin, R. T. (1990). Polarimetric Remote Sensing of
620 Geophysical Media with Layer Random Medium Model. *Progress in Electromagnetics*
621 *Research*, edited by J. A. Kong, Vol. 3, Chap. 1, pp 1-73, Elsevier, New York.
622 Nghiem, S. V., Kwok, R., Kong, J. A., & Shin, R. T. (1993). A Model with Ellipsoidal Scatterers
623 for Polarimetric Remote Sensing of Anisotropic Layered Media. *Radio Sci.*, *28*(5), 687-703.
624 Nghiem, S. V., Kwok, R., Yueh, S. H., & Drinkwater, M. R. (1995). Polarimetric Signatures of
625 Sea Ice, 1, Theoretical Model. *J. Geophys. Res.*, 100(C7), 13665-13679.
626 Nghiem, S. V., & Neumann, (2007). Arctic Sea-Ice Monitoring. *2007 McGraw-Hill Yearbook of*
627 *Science and Technology, 2007*, 12-15, McGraw-Hill, New York.
628 Nghiem, S. V., et al. (2006). Depletion of perennial sea ice in the East Arctic Ocean. *Geophys.*
629 *Res. Lett.*, *33*, L17501, doi:10.1029/2006GL027198.
630 Nghiem, S. V., et al. (2007). Rapid reduction of Arctic perennial sea ice. *Geophys. Res. Lett.*, *34*,
631 L19504, doi:10.1029/2007GL031138.

632 Nghiem, S. V., Clemente-Colón, P., Rigor, I. G., Hall, D. K., & Neumann, G. (2012). Seafloor
633 control on sea ice. *Deep-Sea Res. II − Topical Studies in Oceanography*, *77-80*, 52-61,
634 doi:10.1016/j.dsr2.2012.04.004.
635 Nghiem, S. V., Hall, D. K., Rigor, I. G., Li, P., & Neumann, G. (2014). Effects of Mackenzie
636 River discharge and bathymetry on sea ice in the Beaufort Sea. *Geophys. Res. Lett*., *41*(3),
637 doi:10.1002/2013GL058956.
638 NIC (2015). U.S. National Ice Center and Naval Ice Center sea ice products, available at
639 http://www.natice.noaa.gov/Main_Products.htm, accessed 16 February 2015.
640 Orsi, A. H., Whitworth, T., & Nowlin, W. D. (1995). On the meridional extent and fronts of the
641 Antarctic Circumpolar Current. *Deep-Sea Res*., *42*, 641–673, doi:10.1016/0967-
642 0637(95)00021-W.
643 Ozsoy-Cicek, B., Xie, H., Ackley, S. F., & Ye, K. (2009). Antarctic summer sea ice
644 concentration and extent: comparison of ODEN 2006 ship observations, satellite passive
645 microwave and NIC sea ice charts. *The Cryosphere*, *3*, 1-9.
646 Parish, T. R., & Cassano, J. J. (2003). Diagnosis of the Katabatic Wind Influence on the
647 Wintertime Antarctic Surface Wind Field from Numerical Simulations. *Monthly Weather*
648 *Rev*., *131*, 1128-1139.
649 Parish, T. R., Cassano, J. J., & Seefeldt, M. F. (2006). Characteristics of the Ross Ice Shelf air
650 stream as depicted in Antarctic Mesoscale Prediction System simulations. *J. Geophys. Res*.,
651 *111*, D12109, doi:10.1029/2005JD006185.
652 Park, Y.-H., Vivier, F., Roquet, F., & Kestenare, E. (2009). Direct observations of the ACC
653 transport across the Kerguelen Plateau. *Geophys. Res. Lett*., *36*, L18603,
654 doi:10.1029/2009GL039617.

655 Parkinson, C. L. (2014). Global Sea Ice Coverage from Satellite Data: Annual Cycle and 35-Yr
656 Trends. *J. Clim*., *27*(24), 9377-9382, doi:10.1175/JCLI-D-14-00605.1.
657 Perovich, D. K. (2011). The Changing Arctic Sea Ice Cover. *Oceanography*, *24*(3), 162–173,
658 http://dx.doi.org/10.5670/oceanog.2011.68.
659 Perovich, D. K., et al. (2011) Physical feedbacks and forcings, in *Snow, Water, Ice and*
660 *Permafrost in the Arctic (SWIPA): Climate Change and the Cryosphere*, Section 9.2, Chapter
661 9, pp. 19-30, Arctic Monitoring and Assessment Programme, Oslo, Norway.
662 Perovich, D. K., & Richter-Menge, J. A. (2015). Regional variability in sea ice melt in a
663 changing Arctic. *Phil. Trans. R. Soc. A*., *373*(2045), doi:10.1098/rsta.2014.0165.
664 Reid, P., & Massom, R. A. (2015). Successive Antarctic Sea ice Extent Records during 2012,
665 2013, and 2014. Sidebar 6.3 in "State of the Climate in 2014," *Bull. Amer. Meteor. Soc*.,
666 *96*(7), S163–S214.
667 Rignot, R., Jacobs, S., Mouginot, J., & Scheuchl, B. (2013). Ice-Shelf Melting Around
668 Antarctica. *Science*, *341*, 266-270, doi:10.1126/science.1235798.
669 Sigmond, M., & Fyfe, J. C. (2010). Has the ozone hole contributed to increased Antarctic sea ice
670 extent? *Geophys. Res. Lett*., 37, L18502, doi:10.1029/2010GL044301.
671 Sokolov, S., & Rintoul, S. R. (2002). Structure of Southern Ocean fronts at 140°E. *J. Mar. Syst*.,
672 *37*, 151–184, doi:10.1016/S0924-7963(02)00200-2.
673 Son, S.-W., et al. (2010). Impact of stratospheric ozone on Southern Hemisphere circulation
674 change: A multimodel assessment. *J. Geophys. Res*., *115*, D00M07,
675 doi:10.1029/2010JD014271.

676 Stammerjohn, S., Massom, R., Rind, D., & Martinson, D. (2012). Regions of rapid sea ice
677 change: An inter-hemispheric seasonal comparison. *Geophys. Res. Lett*., *39*, L06501,
678 doi:10.1029/2012GL050874.
679 SPIN (2015). *September Sea Ice Outlook: June Report*. Sea Ice Prediction Network,
680 http://www.arcus.org/sipn/sea-ice-outlook/2015/june, accessed 19 July 2015.
681 Spreen, G., Kaleschke, L., & Heygster, G. (2008). Sea ice remote sensing using AMSR-E 89-
682 GHz channels. *J. Geophys. Res*., 113(C2), 1-14, C02S03, doi:10.1029/2005JC003384.
683 Thorndike, A. S., Rothrock, D. A., Maykut, G. A., & Colony, R. (1975). Thickness distribution
684 of sea ice. *J. Geophys. Res*., *80*(33), 4501-4513, doi:10.1029/JC080i033p04501.
685 Toyota, T., Massom, R., Tateyama, K., Tamura, T., & Fraser, A. (2011). Properties of snow
686 overlying the sea ice off East Antarctica in late winter, 2007. *Deep Sea Res. II*, *58*, 1137-
687 1148, doi: 10.1016/j.dsr2.2010.12.002.
688 Tsai, W.-Y., Nghiem, S. V., Huddleston, J. N., Spencer, M. W., Stiles, B. W., & West, R. D.
689 (2000). Polarimetric scatterometry: A promising technique for improving ocean surface wind
690 measurements. *IEEE Trans. Geosci. Remote Sens*., *38*(4), 1903–1921.
691 Walsh, J. E. (2009). A comparison of Arctic and Antarctic climate change, present and future.
692 *Antarctic Science*, 21(3), 179-188, doi:10.1017/S0954102009001874.
693 Weatherall P., Marks, K. M. Jakobsson, M., Schmitt, T., Tani, S., Arndt, J. E., Rovere, M.,.
694 Chayes, D, Ferrini, V., & Wigley, R. (2015). A new digital bathymetric model of the world's
695 oceans. *Earth and Space Science*, *2*, doi:10.1002/2015EA000107.
696 Webster, M. A., Rigor, I. G., Nghiem, S. V., Kurtz, N. T., Farrell, S. L., Perovich, D. K., &
697 Sturm, M. (2014). Interdecadal changes in snow depth on Arctic sea ice. *J. Geophys. Res.*,
698 *119*, 5395–5406, doi:10.1002/2014JC009985.

699 Webster, M. A., Rigor, I. G., Perovich, D. K., Richter-Menge, J. A., Polashenski, C. M., & Light,
700 B. (2015). Seasonal evolution of melt ponds on Arctic sea ice. *J. Geophys. Res*., *120*(9),
701 5968-5982, doi:10.1002/2015JC011030.
702 Williams, G., et al. (2014). Thick and deformed Antarctic sea ice mapped with autonomous
703 underwater vehicles. *Nature Geosci*., *8*, 61–67, doi:10.1038/ngeo2299.
704 WMO (2014). Sea Ice Nomenclature. *WMO No. 259*, 5th Session of JCOMM Expert Team on
705 Sea Ice.
706 Worby, A. P., Jeffries, M, O., Weeks, W. F., Morris, K., & Jaña, R. (1996). The thickness
707 distribution of sea ice and snow cover during late winter in the Bellingshausen and
708 Amundsen Seas, Antarctica. *J. Geophys. Res*., *101*(22), 28441-28455.
709 World Heritage Encyclopedia (2016), http://www.worldheritage.org/articles/Kerguelen_Plateau,
710 accessed Mar. 2016.
711 Zhang, J. (2007). Increasing Antarctic Sea Ice under Warming Atmospheric and Oceanic
712 Conditions. J. *Clim*., *20*, 2515-2529, doi:10.1175/JCLI4136.1.
713 Zhang, J. (2013). Modeling the Impact of Wind Intensification on Antarctic Sea Ice Volume. *J.*
714 *Clim*., *27*, 202-214, doi:10.1175/JCLI-D-12-00139.1.
715 Zhou, Q. (2013). Circulation and Exchanges at High-latitude Ocean Margins: Dynamical Models
716 and Observations from Instrumented Seals. *Ph. D. Dissertation*, The Arctic University of
717 Norway, Tromsø, available at http://munin.uit.no/handle/10037/5926.
718 Zink, M., & Moirera, A. (2015). TanDEM-X: A Challenging Radar Mission for Generating a
719 New Earth's Topography. pp. 1-4, in *Geomorphology for Geosciences*, Publisher Bogucki
720 Wydawnictwo Naukowe, Adam Mickiewicz University in Poznań - Institute of Geoecology
721 and Geoinformation, Poland.

List of Figures

Fig. 1. Names of places on a map of Antarctic land and ocean together with the GEBCO-2014 bathymetry (http://www.gebco.net/data_and_products/gridded_bathymetry_data/).

Fig. 2. Tracking of trajectories of sea ice parcels over different synoptic sea ice classes (see definitions in Section 4 and color code in Fig. 4). The left panel (a) represents the initial set of points in a 2^o grid on sea ice for 1 June 2008 to track the sea ice parcels associated with this set of points to track their trajectories while no new points are introduced or inserted throughout the tracking process. The right panel (b) shows the trajectories of the sea ice parcels at the end of the tracking on the equinox of 22 September 2008, tracing the entire history of the trajectory of each sea ice parcel from where it started, moved around, reached its final position. Red dots are the current positions of the trajectories on the given date with the orange trails indicating the drift of the tracks during the past 30 days and the trails consisting of small black dots completing all tracking points along the sea ice tracks since 1 June 2008. An animation of the daily sea ice trajectories is presented in Movie 1 at http://urban.jpl.nasa.gov/images/NghiemEtAl-Movie1.avi.

Fig. 3. Radar backscatter patterns and transect plots of Antarctic sea ice observations in 2008 by the QuikSCAT satellite scatterometer operated at the Ku-band frequency of 13.4 GHz. The top left insets are for QuikSCAT backscatter of sea ice on 22 June and 22 September 2008, where the color scale is for backscatter values, blue for ocean, grey for permanent ice, and brown for land. The backscatter plots are for (a) Transect a along 3.38^oE, (b) Transect b along 45.0^oE, (c) Transect c along 176.62^oW, (d) Transect d along 135.0^oW, and (e) Transect e along 30.0^oW. The plot colors are green for June, magenta for July, blue for August, and black for September.

Fig. 4. Synoptic classes of Antarctic sea ice around the September equinox in 1999-2009. The location of Bouvet Island is marked with the white cross.

745 **Fig. 5.** Antarctic sea ice trajectories overlaid on maps of synoptic sea ice classes on 22 June,
746 July, August, and September 2008. Red dots are the current positions of the trajectories on the
747 given date with the orange trails indicating the drift of the tracks during the past 30 days and the
748 trails consisting of small black dots completing all tracking points along the sea ice tracks since 1
749 June 2008. The color code for open water and sea ice classification is the same as in Figure 4.
750 Dark grey represents land. The location of Bouvet Island is marked with the white cross.

751 **Fig. 6.** Air temperature measured at Bouvet Island, obtained from the National Oceanic and
752 Atmospheric Administration (NOAA) Global Surface Summary of the Day (GSOD) dataset
753 (https://data.noaa.gov/dataset/global-surface-summary-of-the-day-gsod). The horizontal axis is
754 for number of days counted from 1 January 1994 (1 is for 1 January 1994, 366 is for 1 January
755 1995, etc.). This uninhabited island is located near a triple junction on the southern end of the
756 Mid-Atlantic Ridge. It is the most remote island in the world with more than 1,600 km away
757 from the nearest land in any direction.

758 **Fig. 7.** Maps of Multi-sensor Ultra-high Resolution (MUR) Sea Surface Temperature (SST)
759 represented by the color bar in degrees Celsius on the right with isotherms at -1.0^{o}C (black
760 contour) and -1.4^{o}C (green contour) on National Ice Center (NIC) Sea Ice Extent (SIE) mask in
761 maroon for: (a) 22 September 2008, and (b) 22 September 2009. The white cross marks the
762 location of Bouvet Island.

763 **Fig. 8.** Map of the southern Antarctic Circumpolar Current (ACC) front (sACCf) delineated by
764 the white contour (Kim and Orsi, 2014) with MUR SST -1.0^{o}C isotherms represented by the
765 black contours on 22 September in 2002-2009 plotted together with the GEBCO-2014
766 bathymetry. The isotherms are closely bundled close to the sACCf over pronounced seafloor

767 features such as ridges while they tend to spread apart across smooth abyssal plains. The white
768 cross marks the location of Bouvet Island.

769 **Fig. 9.** Map of MUR SST −1.0°C isotherms as black contours on 22 September in 2002-2009 on
770 the GEBCO-2014 bathymetry in the region of the Kerguelen Plateau, a submerged
771 microcontinent. The isotherms closely bundle as they pass across the Kerguelen Plateau through
772 the Fawn Trough. However, the isotherms tend to spread apart over the deep Enderby Basin and
773 the deep Australian Antarctic Basin where seafloor features are not pronounced.

774

775 **List of Tables**

776 **Table 1.** Frontal ice zone (FIZ) distances and widths along different longitudes on 22 July, 22
777 August, and 22 September 2008. The FIZ distance is between the coastline (or the outer edge of
778 Ross ice shelf) and the inner edge of FIZ. The FIZ width is between the inner and outer edges of
779 the FIZ. The uncertainty in the FIZ distance and FIZ width is ±25 km.

780

781 **List of Movies**

782 **Movie 1.** Movie of Antarctic sea ice trajectories, derived from QuikSCAT satellite data, overlaid
783 on daily maps of synoptic sea ice classes. An initial set of starting points in a 2° grid on sea ice
784 for 1 June 2008 is chosen and then tracked until 30 September 2008. Red dots are the current
785 positions of the trajectories on each given date. The orange trails indicating the drift of the tracks
786 during the past 30 days, and the trails consisting of small black dots completing all tracking
787 points along the sea ice tracks since 1 June 2008. The color code for open water and sea ice

788 classification is the same as in Fig. 4. Dark grey represents land. The location of Bouvet Island
789 is marked with the white cross.